Effects of fluctuations in concentration on detonation propagation

Yong Zhou (周泳)[1], Xiaojun Zhang (张晓军) [1,*], Lijia Zhong (钟力嘉)[1], Ralf Deiterding[2], Lei Zhou (周磊)[1,*]，Haiqiao Wei (卫海桥)[1]

1 State Key Laboratory of Engines, Tianjin University, Tianjin 300072, China

2 Aerodynamics and Flight Mechanics Research Group, University of Southampton, Boldrewood Innovation Campus, Southampton SO167QF, United Kingdom

*Corresponding author:

Email: lei.zhou@tju.edu.cn (Lei Zhou); xjzhang@tju.edu.cn (Xiaojun Zhang)

Abstract

The authors examine the effects of inhomogeneity in the equivalence ratio on detonation propagation by using a set of two-dimensional numerical simulations of the detailed reaction chemistry of an H_2/air mixture. A random field of fluctuations but with statistical characteristics is introduced, and several combinations of the root mean square (RMS) and characteristic length scales of the fluctuations are considered to investigate the evolutions of the cellular structure, speed of detonation, and shock pressure under these setups. The results indicate that an increase in the RMS enlarged the cell formed by the original triple points as well as the characteristic length scale to promote the transition from a single cellular pattern to a double cellular pattern. The large cell of the double cellular pattern was formed by triple points generated from local explosion, and the decoupling or curvature of the detonation wave within an extremely lean region was important for this process. Moreover, sustainable detonation propagation under these configurations benefited from the strong transverse detonation generated by the local explosion as well as the propagation of these original triple points along the stoichiometric region, where their collisions reinitiated detonation in the extremely lean region. The instantaneous and average speeds of detonation were calculated. The former followed the trend of evolution of the normalized potential instantaneous energy release, whereas the latter decreased with an increase in $\emptyset'$. However, the value of $l_{\emptyset}$ had a non-monotonic influence that can be attributed to two factors.

Keywords: Detonation propagation; Inhomogeneity; Cellular structure

1. Introduction

Deflagration-to-detonation transition (DDT) is a fundamental physical phenomenon in astrophysics, cosmology, detonation engines, and the explosion of vapor clouds.[1-3] Detonation propagation has received extensive attention in recent years because controlled detonation propagation can potentially revolutionize the propulsion system, e.g., in a rotating detonation engine

(RDE)[4, 5], while uncontrolled detonation propagation, e.g., gas explosions in mining operations and super-knocks in highly boosted gasoline engines,[6] may lead to accidental explosions that threaten safety. In these scenarios, a mixture with local high/low equivalence ratio pockets may form owing to the insufficient mixing of air and fuel.[7] The detonation may become unstable as it interacts with the inhomogeneous mixture. Therefore, it is important to characterize the dynamics of detonation propagation in an inhomogeneous mixture.

Many studies have extensively explored detonation propagation in inhomogeneous mixtures. The first popular scenario that has been investigated in this vein is one in which a detonation propagates through the mixture with a concentration gradient parallel to the direction of propagation.[8-13] In an early study, Thomas et al.[11] experimentally observed that the cellular structure adjusts rapidly to local concentration conditions when a detonation moves across the mixture with a continuously decreasing reactivity gradient. More details of the decay of detonation and its reinitiation within such a concentration configuration were recently uncovered by Honhar et al.[13] through numerical simulations. In multiple dimensions, a partially failed detonation develops within the region of the gradient that consists of overdriven detonation, and the complex of decoupled shock and the reaction zone. Strong transverse detonation, propagating from the overdriven region to the failed region, is key to the survival of detonation under such conditions. The other common setup considered within this scenario involves the insertion of one or multiple inert layers into the reactive mixture. The critical thickness of the inert layer, beyond which a detonation fails to be reinitiated, is of great interest in these configurations.[10, 12] Tang et al.[10] noted that the critical thickness, when normalized by the length of the Zel'dovich–von Neumann–Döring (ZND) induction, asymptotically decreases with an increase in the effective activation energy.

The second scenario of detonation propagation in inhomogeneous mixtures involves a reactivity gradient that is perpendicular to detonation propagation. Several valuable findings on detonation dynamics and the cellular structure have been obtained by using these gradient profiles in both numerical and experimental studies.[14-20] First, an inclined detonation front appears in the mixture with a transverse concentration gradient, and Mach reflection occurs in the lean region when the gradient is steepened, which in turn increases the pressure-induced load on the adjacent wall. Secondly, the motion of the triple points along the tilted detonation front forms parallelogram cellular structure rather than diamond ones, and steepening the gradient leads to multi-head detonation to single-head detonation transition. Lastly, the average deficit in the detonation velocity relative to the Chapman–Jouguet (CJ) speed increases with the gradient because of the delay in the downstream reaction reaching equilibrium.

In contrast to the above two scenarios involving a one-dimensional (1D) gradient, the third

considers detonation propagation in a mixture with nonlinear and 2D periodic disturbance. Few studies have focused on this scenario. Wang et al.[21] numerically investigated the effects of a periodic 2D sinusoidal distribution of reactant concentration on detonation propagation. Mi et al.[22-24] examined detonation propagation in a mixture with spatially discretized energy sources, where super-CJ detonation was identified which an average wave speed higher than the CJ speed. Prakash et al.[4] and Cuadra et al.[25] investigated the effects of fluctuations in reactivity on the average structure of the detonation. However, our understanding of the evolution of the cellular pattern and the dynamics of detonation propagation remains limited.

While recognizing the value of the above studies, they have primarily considered detonation propagation in inhomogeneous mixtures with relatively regular disturbances (i.e., 1D gradient or periodic sinusoidal), and details of the reaction mechanism have not commonly been examined. Thus, we introduce a series of inhomogeneous concentration fields that are random but have statistical characteristics in this study to examine the evolution of the dynamics of detonation and the cellular structure through a set of 2D simulations while considering the detailed chemistry of the reaction. This is the first study of its kind, to the best of our knowledge.

2. Computational configurations and numerical methods

2.1 Computational configurations

As shown in **Fig. 1**, a set of 2D rectangular domains with length $L = 18.8$ cm and height $H = 6.4$ cm were considered and divided into two sections: a homogenous region on the left with a stoichiometric hydrogen (H_2)/air mixture and length $L_0 = 6$ cm, and an inhomogeneous region on the right with random fluctuations in the equivalence ratio. An initial pressure of $P_0 = 1$ atm and temperature of $T_0 = 300$ K were imposed in the entire domain. A ZND profile, with the same initial conditions as those of the homogenous region, was placed at the left end to ignite a detonation that propagated rightward. Outflow boundary conditions were applied to the left and right boundaries, and periodic boundary conditions were used on the upper and lower boundaries so that the effect of the wall was eliminated.

Initial fluctuations in the equivalence ratio were generated by using the synthesized turbulence approach[26, 27] originally designed to generate isotropic turbulence (velocity field). The desired field could be obtained by substituting velocity with the equivalence ratio in the related formula (note that the mixture was initially quiescent, and the method was applied here to generate fluctuations only in the equivalence ratio). The localized mass fraction ratio of H_2:O_2 was then calculated from the equivalence ratio while the mole ratio of O_2 to N_2 is fixed at 1:3.76. A similar method has been widely used to examine the effects of inhomogeneity on ignition.[28-30] Two basic parameters were added in

this method: the root mean square (RMS) of fluctuations in the equivalence ratio $\emptyset'$ and the characteristic length scale $l_{\emptyset}$. A larger $\emptyset'$ yielded a wider range of equivalence ratios in the field (i.e., a smaller lower limit or a larger upper limit). Increasing $l_{\emptyset}$ enlarged the rich/lean pockets. Several combinations of $\emptyset'$ and $l_{\emptyset}$ were considered in the simulations and are summarized in **Table 1**. The initial fields of the equivalence ratio for these cases are provided in the Section A.1 in the Appendix for reference. Because the initial temperature and pressure were constant, the density varied with the composition of the mixture according to the equation of state. The mean equivalence ratio for all cases was one, and values of the global energy and reactivity were consistent with the stoichiometric mixture.

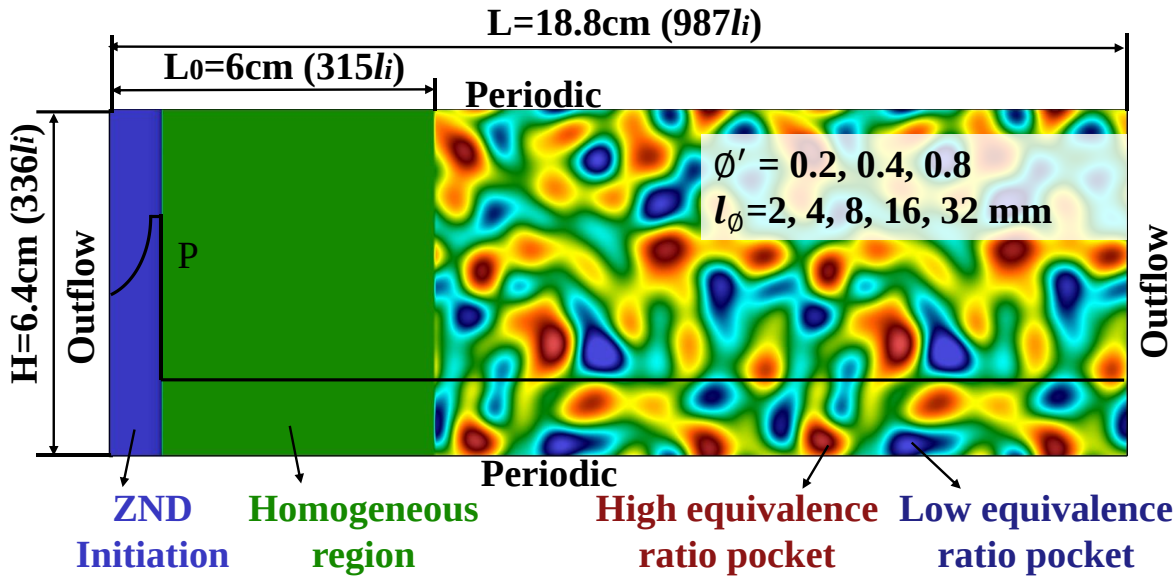

Fig. 1 Computational model.

Table I

Cases considered in the simulations

Case	$\emptyset'$	$l_{\emptyset}$ (mm)	Range of $\emptyset$
1	0.2	2	0.2–1.91
2	0.4	2	0.02–2.75
3	0.8	2	0.06–4.54
4	0.4	4	0.02–3
5	0.4	8	0.02–2.38
6	0.4	16	0.02–2.338
7	0.4	32	0.08–2.01

2.2 Numerical methods

The reactive compressible Navier-Stokes (NS) equations are solved in the present simulations by the parallel adaptive mesh refinement framework AMROC[31]. The time-operator splitting approach, Godunov splitting, is utilized to decouple hydrodynamic transport and chemical reaction source term. The convective parts and diffusion terms are discretized by MUSCL-TVD scheme with hybrid Riemann solver and second-order accurate central difference scheme respectively, while the reactive source term is solved by 4th order semi-implicit Runge-Kutta method GRK4A. The thermodynamic properties, transport parameters and reaction rate are evaluated by the Chemkin library linked to AMROC. A detailed reaction mechanism of Li et al.[32] for H_2/air mixture is utilized in the present work. With adaptive mesh refinement method, AMROC can accurately resolve the flame front, shock wave and detonation, and thus has been successfully applied to extensive studies of flame propagation and detonation[10, 21, 33-36]. The base grid size is $250\ \mu m$ and five additional refinement levels are utilized, giving the finest mesh size of $7.8\ \mu m$, corresponding to 24 mesh points per induction length ($l_i = 0.19$ mm). The detail assessment of the grid convergence is provided in the section A.2 in Appendix.

3. Results and discussion

3.1 Global cellular structures

Fig. 2 shows the evolution of the cellular structures, along the effects of the RMS of fluctuations in the equivalence ratio. A larger cellular size was observed as the detonation propagated into the inhomogeneous mixture in all cases. The greater the RMS was, the greater the extent to which the size increased. For $\emptyset' = 0.2$ and 0.4, the detonation cell was relatively regular, and became much more distorted as $\emptyset'$ was increased to 0.8. The increase in cell size was directly related to the decrease in the number of triple points as the pressure contours on the right show in **Fig. 2**. This has been also observed in studies on detonation propagation with a transverse gradient.[14, 18, 19] Cell size is an intrinsic characteristic of detonation waves. It usually reaches the minimum value when the mixture is stoichiometric, and both a leaner and a richer mixture have large cells.[37] As the detonation propagated from the homogenous to the inhomogeneous region, some triple points interacting with the local lean or rich mixture weakened and even disappeared to decrease in number. In this present configuration, the increase in the RMS raised the ratios of extremely lean and rich mixtures to enhance the likelihood of decay of the triple points. As a result, the cell size increased with the RMS. A more wrinkled wave front was induced by the large inhomogeneity at $\emptyset' = 0.8$, and the motion of the triple points along it led to a more irregular and distorted cellular structure. In addition, the cell size in the

homogenous mixture was about 0.7 mm in the simulations, much smaller than those measured in the experiments[37] of about 10 mm for the same initial conditions. Considering the importance of cell size in this study, the same simulations were executed by using the chemical mechanism due to Westbrook[38] to check if the conclusions were independent of the mechanism involved. The results as well as a detailed discussion of cell size are presented in Section A.3 of the Appendix.

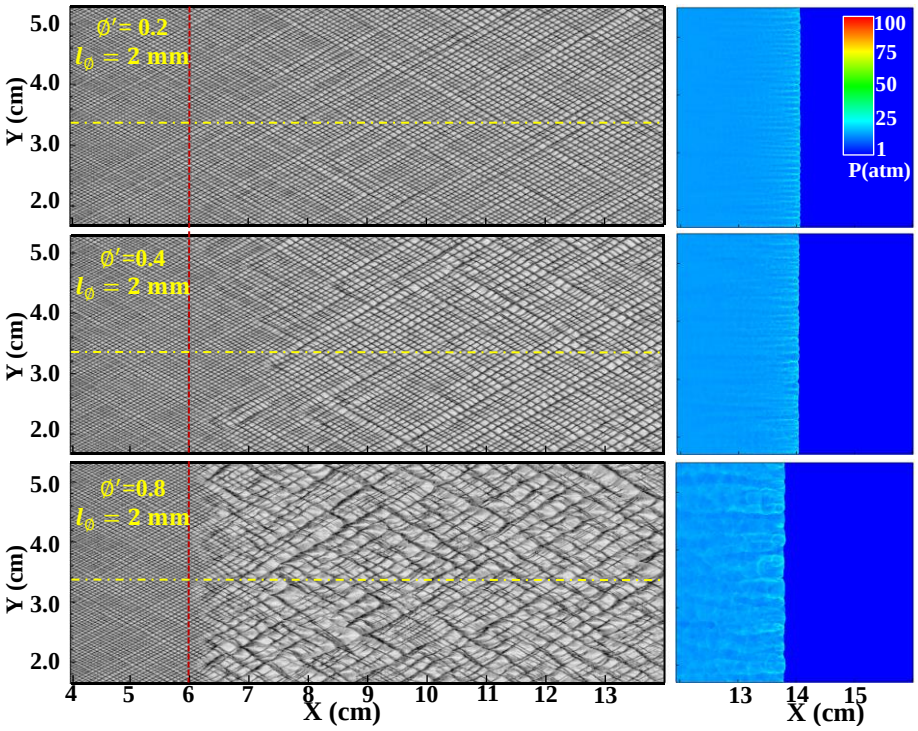

Fig. 2 Numerical soot foils for $\emptyset' = 0.2, 0.4$, and 0.8 (from top to bottom) with a fixed $l_\emptyset = 2$ mm, along with pressure contours at t=64.25 μs to the right. The red lines demarcate the homogeneous and inhomogeneous regions. The yellow line, placed at $Y = 3.37$ cm, is used for the subsequent pressure analysis.

More interesting cellular patterns formed when the characteristic length scale $l_\emptyset$ increased, as shown in **Fig. 3**. First, in contrast to the nearly uniform cellular structure in case 2 with $\emptyset' = 0.4$ and $l_\emptyset = 2$ mm, some scar-like structures appeared when $l_\emptyset$ was increased to 4 mm, and was aggravated at $l_\emptyset = 8$ mm to lead to a fairly chaotic pattern in this case. However, the situation changed as $l_\emptyset$ rose to 16 mm, and the cells were reorganized to form a sophisticated double cellular pattern, e.g., as indicated by the zone circled by the diamond "ABCD." As discussed in the next section, small cells within the diamond originated from the intrinsic instability of detonation, and their size was determined by the induction length of the mixture. We call them the original triple points. The formation of the large cells was closely related to the motion of the triple points induced by localized

extremely lean pockets, and there were different reasons for the generation of these triple points (as is discussed in the next section). As $l_{\emptyset}$ was further increased to 32 mm, the large cells seemed to not be able to sufficiently develop in the computational domain, which implies that the large cell size was positively related to $l_{\emptyset}$. In addition, increasing $l_{\emptyset}$ led to a more curved detonation front.

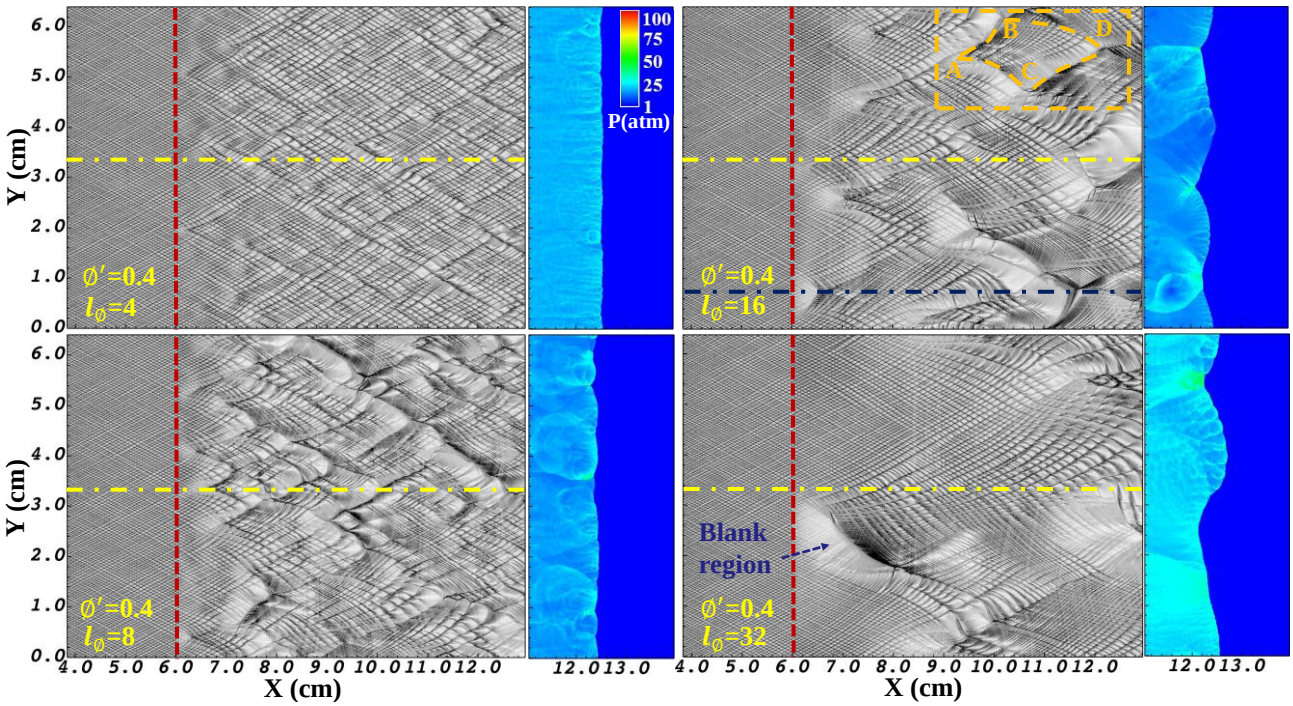

Fig. 3 Numerical soot foils and for $l_{\emptyset} = 4, 8, 16$ and 32 mm with the fixed ∅′=0.4, along with the pressure contours at t=56.75μs at the right. The yellow lines represent the trajectories of the secondary triple points. The yellow line located at $Y = 3.37$ cm and the blue line located at $Y = 0.75$ cm are used the later pressure analysis. The diamond ABCD shows a double cellular pattern and the box zone is explored in detail in the next section.

3.2 Formation of double cellular pattern

To interpret the formation of the double cellular pattern, **Fig. 4** shows the evolution of contours of the mass fraction of H_2 overlaid with the density gradient within the orange box in **Fig. 3** at different times. The process began with the diamond vertex A. At $t = 42.5$ μs, a concave and partially decoupled shock front appeared before reaching the rich region I because it had just passed through an extremely lean region with the lowest equivalence ratio of $\emptyset = 0.024$. The concave shock front caused multiple tripe points to converged on the trough of the wave, leading to a locally drastic rise in pressure. Consequently, once the leading shock moved into the region where ∅ was close to one, a local explosion was triggered, as shown by the temperature insert at $t = 42.5$ μs, that reinitiated the

local detonation. Two strong triple points TP1 and TP2 were formed, and propagated upward and downward along the front, respectively. After passing through the rich region I, a region of decoupling emerged above TP1 at $t = 45.75$ μs, and initiated a transverse detonation that propagated upward with a peak pressure of over 100 atm, as shown by the pressure insert. A similar phenomenon was observed by Honhar et al.[13] whereby a detonation transmitted across a reactivity gradient parallel to the direction of propagation, with the difference that the overdriven detonation here originated from the local explosion induced by the localized lean mixture. Meanwhile, the other triple point TP3 moved downward along the stoichiometric region between regions I and II, and then interacted with TP1 at vertex B at $t = 46.5$ μs. They consumed the unburnt mixture of the decoupling region and redetonated there. Tracing the history of TP3 before 45.75 μs reveals that it should have been an original triple point. In the lower part of the diamond, TP2 moved downward and approached the other triple point TP4 that propagated upward, as shown in the insert at $t = 48.5$ μs. An observation (not shown here) showed that the strength of TP4 suddenly increased before 48.5 μs because it entered the stoichiometric region between regions III and IV, and was fed by the locally abundant energy release. In addition to TP3 and TP4, the increase in the number of triple points propagating along the stoichiometric region was a common feature in this configuration. TP2 and TP4 collided at 49 μs and formed the vertex C. Their collision promoted the local reaction, which further increased their strength. The lower part of the detonation front between TP3 and TP2 was decoupled as it interacted with the lean region III. At $t = 56.5$ μs, the downward-directed TP3 met the upward-moving TP4 at vertex D, which finally enclosed the diamond and a robust detonation formed within the selected window. In addition, the original triple points also existed simultaneously along the wave front when the triple points mentioned above propagated, especially at 46.5 and 56.5 μs, to construct substructures within the diamond.

Therefore, the collision between the transverse detonation induced by the local explosion and the original triple points propagating along the stoichiometric region reinitiated the detonation in the extremely lean region and thus sustained its survival under the given configurations. It is noteworthy that the concave wave front is not the only way to generate local explosion or transverse detonation, and two other ways are shown in **Fig. 5**. The first involves a double-transverse wave collision. As shown in the first row, a decoupled wave front appeared as it entered a lean region at $t = 24.5$ μs in case 6 ($l_{\emptyset} = 16$ mm). However, the front remained flat, and thus no convergence of the triple points was observed. After it passed through the stoichiometric region and interacted with the rich pocket, two transverse waves were formed at the top and bottom of the window and propagated toward each other. They collided and reinitiated the detonation at $t = 27.5$ μs. The second way to generate local explosion or transverse detonation involve the propagation of a single transverse wave. As shown in

the second row for case 7 ($l_{\emptyset} = 32$ mm), a flat and decoupled wave front was generated after it entered the lean region, and a transverse detonation (with a peak pressure of over 100 atm) was then produced and propagated downward closely along the line of the stoichiometric contour. It consumed the unburnt mixture behind the leading shock and redetonated there. This manner of generation is most similar to that observed by Honhar et al.,[13] and is reasonable because the large pocket in case 7 could have provided a comparable gradient distribution to that reported in their work. These three ways make a major contribution to the redetonation of the decoupled front and the sustenance of the detonation in these configurations. Note that cases 6 and 7 are used as examples here, and these means of formation were observed at other locations and in the other cases as well.

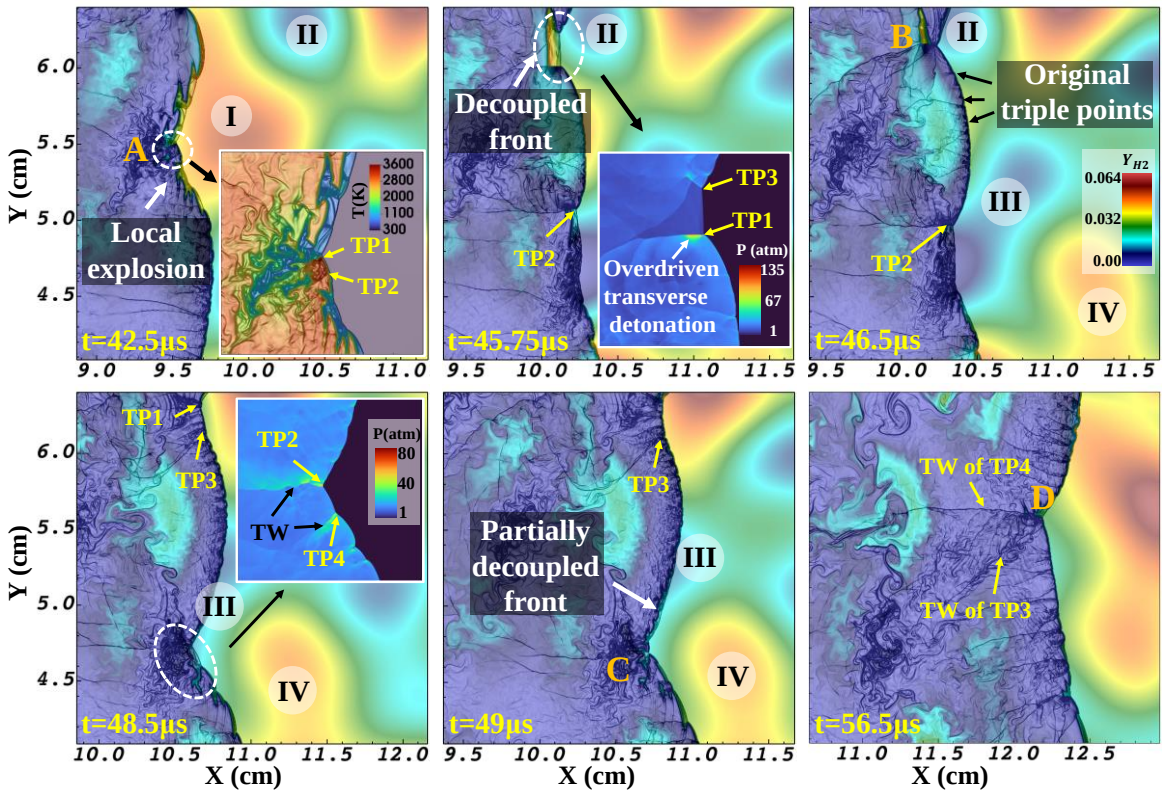

Fig. 4 Evolution of contours of the mass fraction of hydrogen overlaid with the density gradient within the orange box in Fig. 3 at different times for $\emptyset'$=0.4. The stoichiometric region corresponds to dark green. Regions I and IV are rich pockets, and regions II and III are lean pockets. TP: triple point; TW: transverse wave.

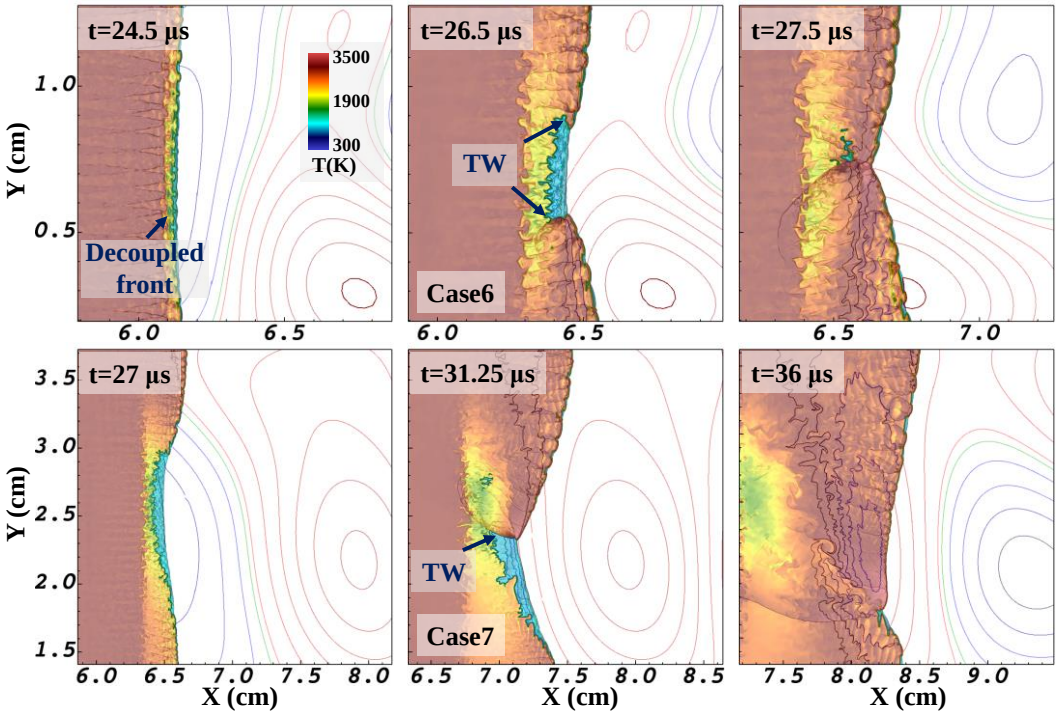

Fig. 5 Different ways for triggering the local explosion and overdriven transverse detonation. The first row represents case 6 ($l_{\emptyset} = 16$ mm) and the second row case 7 ($l_{\emptyset} = 32$ mm). The temperature contour is overlaid with the density gradient and combined with the contour lines of the mass fraction of H_2.

3.3 Effects of $l_{\emptyset}$ and $\emptyset'$

The above analysis reveals that the coexistence of the original triple points and the triple points induced by local explosion is important for the formation of the double cellular pattern. When both $l_{\emptyset}$ and $\emptyset'$ were relatively small, the inhomogeneity had a slight influence on the detonation and the wave front remained nearly flat, as shown in **Fig. 2**. Thus, local explosions rarely occurred in cases 1 and 2 owing to a lack of focus of the multiple triple points, and only cells formed by the motion of the original triple points emerged. Meanwhile, triple points entering the extremely lean region might have disappeared, which led an increase in cell size increase with $\emptyset'$. With a further increase in $\emptyset'$ to 0.8, the ratios of the extremely lean and rich regions increased, and wrinkles appeared at the wave front and triggered a series of local explosions. The explosions were dense, and the distance between adjacent ones was small, which implies that the induced increases in cell size were relatively small. On the contrary, the cell size generated by the original triple points further increased for the reason mentioned above. These two effects might have resulted in a comparable size between these types of triple points. Therefore, the double cellular pattern did not appear in this case. Nevertheless,

increasing $l_{\emptyset}$ directly enlarged pockets that had the ability to locally decay the detonation, resulting in a more violent curvature along the wave front and a consequent enhancement of the local explosions. This can be verified by the "blank" regions in the soot foils of **Fig. 3** that correspond to an extremely lean local region. Thus, the detonation was decoupled and no triple point was captured. The size of a single "blank" region mostly increased as $l_{\emptyset}$ rose from 4 mm to 32 mm and the wave front became more curved. On the contrary, the increase in $l_{\emptyset}$ also reduced the number of pockets when the space was fixed, and thus increased the distance between adjacent explosions. This yielded a much larger cell than that formed by the original triple points. Finally, the double cellular pattern appeared. In addition, we called case 5 with $l_{\emptyset} = 8$ mm a chaotic pattern in Section 3.1. In fact, these scar-like structures were underdeveloped larger cells. Owing to the random distribution of the rich/lean pockets, one triple point might have decayed before it collided with the other one, which left these random "scars." Lastly, attending to these substructures shows that the cell size changed smoothly, e.g., from small to large, within some localized regions. It was formed by the propagation of triple points along a curved wave front, e.g., the distance between the triple points moving along an expanded front increased, as did the cell size. In addition, the local decay of some triple points also led to a larger cell size.

3.4 Pressure analysis

The histories of shock pressure along the lines of $Y = 3.37$ cm for the representative cases and $Y = 0.75$ cm for case 6 are shown in **Fig. 6**. Note that the locations were artificially selected in order to better explain the double cellular pattern and the strength of the corresponding triple points. Several observations can be made. First, the shock-induced pressure oscillated within a region of 20–50 atm without the double cellular pattern in cases 1 and 2, and a much larger peak pressure appeared in case 3 to confirm the occurrence of the local explosion. Second, the shock-induced pressures corresponding to the substructure of cases 5–7 were almost the same as those of cases 1 and 2, although double cellular pattern occurred in the former. Lastly, a decoupled region with pressure continuously below the P_{VN} of the stoichiometric mixture is captured in **Fig. 6**(c), and corresponds to the blank zone in **Fig. 3** for case 6, which is consistent with our previous description. A peak pressure of over 100 atm was also observed that was related to a local explosion. These observations again show that the triple points generated by the aforementioned three means were much stronger than the original triple points, and had the ability to propagate through the relatively lean or rich region and redetonate the local decoupled wave front, which satisfied an essential requirement for the sustainable propagation of detonation. Although the original triple points easily decayed in the lean region, some of those propagating along the stoichiometric region strengthened, and their collision with the triple

points from the explosion provided an additional guarantee of the survival of detonation.

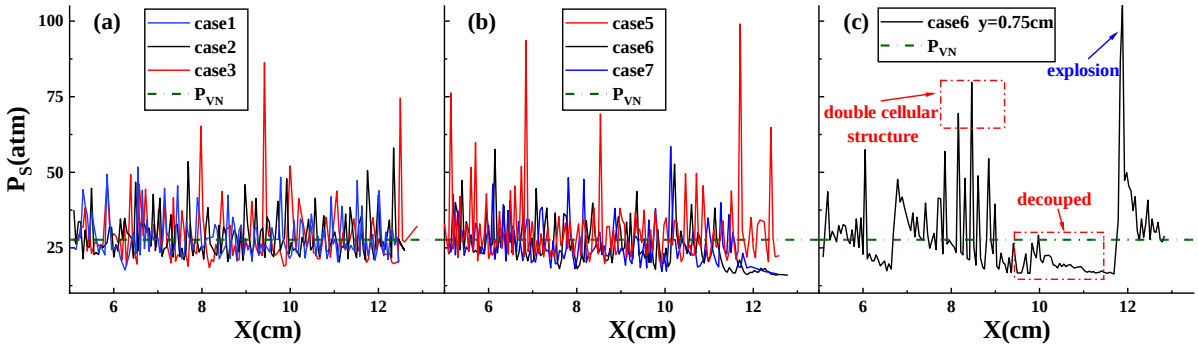

Fig. 6 Histories of shock-induced pressure along the lines of Y = 3.37 cm (a) for cases 1, 2, and 3, (b) cases 5, 6, and 7, (c) and case 6 with Y = 3.37 cm (the corresponding locations are marked in Fig. 2 and Fig. 3). The P_{VN} for stoichiometric mixture is plotted as a reference.

3.5 Velocity analysis

Fig. 7 shows the instantaneous speeds of detonation normalized by the CJ speed for $\emptyset$ =1 in different cases. The instantaneous speeds are defined as the temporal derivatives of the average position of the detonation front, which was obtained by the integral of the localized position of the detonation front across the entire channel divided by the height of the channel at the time, i.e.,

$$V_{\text{shock}} = \frac{Dx_{\text{avg}}}{Dt} = \frac{D}{Dt}\left[\frac{1}{H}\int_{y_1=0}^{y_2=6.4} x(y,t)dy\right]$$

where x is the localized position of the detonation front. It shows that compared with $\emptyset'$, $l_{\emptyset}$ had a greater influence on the frequency and amplitude of oscillations in the instantaneous speeds of the wave. Also shown in **Fig. 7** are the evolutions of the normalized potential instantaneous release of energy. It is called "potential" because it was determined by the field of the initial equivalence ratio rather than real-time heat release. Therefore, it reflects energy support from the initially well-premixed mixture. Specifically, it was calculated by

$$\text{Normalized potential instantaneous energy release} = \frac{1}{V}\iiint MdV$$

$$\text{where } M = \begin{cases} \dfrac{(\rho Y_{H_2})_{local}}{(\rho Y_{H_2})_{stoic}}, & \text{for lean region} \\ \dfrac{(\rho Y_{O_2})_{local}}{(\rho Y_{O_2})_{stoic}}, & \text{for rich region} \end{cases}$$

where V is the volume of the region covered by the detonation front, $(\rho Y_{H_2})_{local}$ and $(\rho Y_{O_2})_{local}$ are

the localized initial mass densities of hydrogen and oxygen in the corresponding region, respectively, and $(\rho Y_{H_2})_{stoic}$ and $(\rho Y_{O_2})_{stoic}$ are their mass densities in the stoichiometric H_2/air mixture. All cases show that the instantaneous speeds of detonation followed the trend of evolution of the normalized potential instantaneous energy release, which means that energy support from the initially well-premixed mixture played a crucial role in the evolution of the instantaneous speeds of detonation.

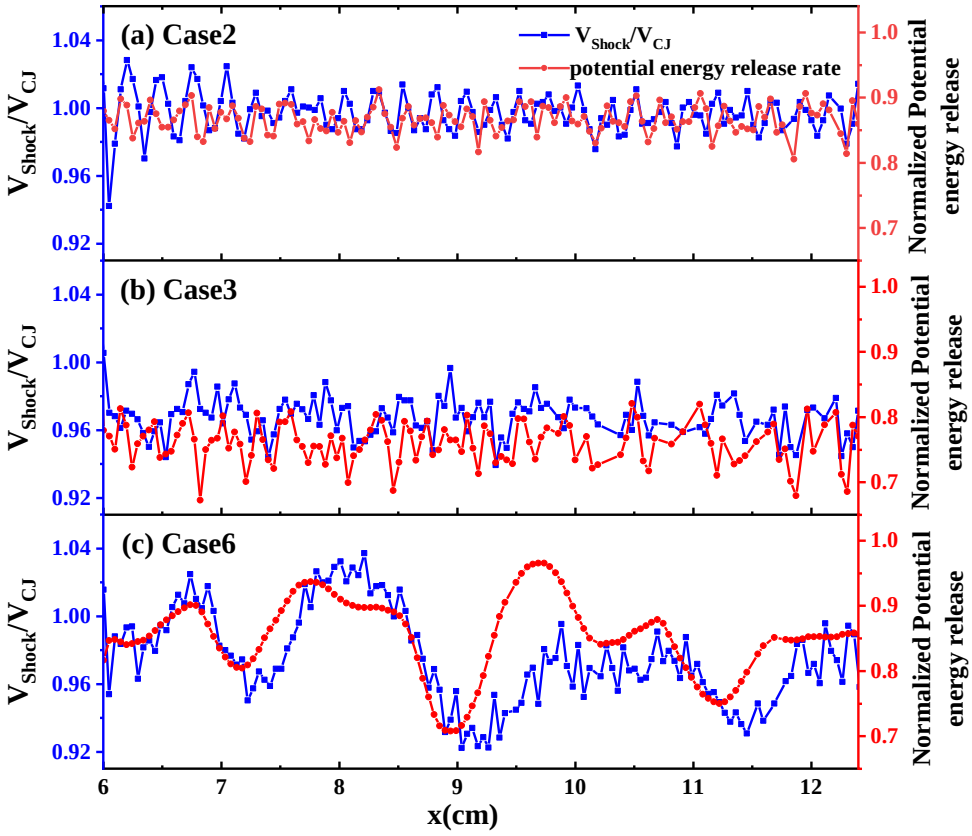

Fig. 7 Profiles of instantaneous speeds of detonation and potential instantaneous energy release as a function of the average wave position in different cases. (a) Case2. (b) Case3. (c) Case 6.

Fig. 8 shows the normalized average speed of detonation and the normalized total potential energy release within the region swept by detonation in all cases. The start position for calculation was $x_0 = 6$ cm, and six end positions were selected to ensure that the results were independent of the measurement position. The results are represented by the error bar. It is clear that the average speeds of detonation in all cases were lower than the stoichiometric CJ speed except some measurements for $l_\emptyset = 2$ mm and $\emptyset' = 0.2$. The higher value occurred because the propagation of detonation in the homogenous region was slightly overdriven, and the small $\emptyset' = 0.2$ caused only a minor deficit in its speed when it just entered the inhomogeneous region. The average speed decreased to become lower

than the CJ speed as the measurement position moved gradually away from the start position. Detonations propagating at an average speed lower than the CJ speed in inhomogeneous mixtures have been observed in previous studies on inhomogeneity.[18, 19, 21] Under inhomogeneous conditions, two main factors are responsible for the velocity of detonation. One is the potential energy released from the initially well-premixed mixture that can immediately feed the detonation, as we have discussed in the context of instantaneous speed. The other is determined by the extent to which the extra H_2 in the rich mixture and O_2 in the lean region diffuse to form a combustible mixture to support detonation propagation. To illustrate this, the 1D Favre-averaged detonation profile in a wave-attached reference frame moving at a speed of V_{avg} was calculated for $l_{\emptyset} = 16\ \mathrm{mm}$, and was discussed in detail in Section 3.2. The mathematical scheme used was similar to that by Radulescu et al.,[39] who showed that such a structure is a meaningful concept for analyzing the chemical and hydrodynamic equilibria of unstable detonation. As shown in **Fig. 9**, the mass fraction of hydrogen reached the CJ state 3.5 cm behind the shock, farther than the mean sonic point at 0.725 cm, which means that chemical equilibrium was not reached at the sonic point and, thus, part of the energy released could not feed the detonation propagation. This eventually led to a reduction in the speed of detonation.

In addition, the deficit in speed increased with the an increase in $\emptyset'$ at a fixed $l_{\emptyset}$, as shown in **Fig. 8** (a). When $l_{\emptyset}$ was fixed, the distribution (i.e., the size and the position) of these lean and rich pockets was the same for the three cases, and only oscillations in the amplitude of $\emptyset$ increased with $\emptyset'$, as shown by the initial equivalence ratio fields in the Appendix. On the one hand, this led to a reduction in the total potential energy release, as shown in **Fig. 8** (a), and on the other hand, it extended the time for the mixing of the extra H_2 and O_2 to form a combustible mixture during detonation propagation to enhance the energy losses and deficit in the speed of detonation. However, the effects of $l_{\emptyset}$ on average speed were non-monotonic as shown in **Fig. 8** (b). The deficit in speed reached its maximum value at $l_{\emptyset} = 8\ \mathrm{mm}$. Although it seems that the speed of evolution followed the trend of the total potential energy release, their absolute value did not match. For example, case with $l_{\emptyset} = 2\ \mathrm{mm}$ and $l_{\emptyset} = 4\ \mathrm{mm}$ had higher average speeds than those with $l_{\emptyset} = 16\ \mathrm{mm}$ and $l_{\emptyset} = 32\ \mathrm{mm}$, but the potential energy releases in the former cases were smaller than in the latter. Different values of $l_{\emptyset}$ changed the distribution of these lean and rich pockets. For $l_{\emptyset} = 2\ \mathrm{mm}$ and $4\ \mathrm{mm}$ with a small pocket, the extra H_2 and O_2 attained better and faster turbulent mixing induced by the motion of the triple points, which provided energy to support detonation propagation. However, for $l_{\emptyset} = 8\ \mathrm{mm}$, although better mixing was obtained, it was not sufficient to compensate for the difference in potential energy release, leading to the minimum value. A detailed analysis of the interaction between turbulent mixing and fluctuations in the equivalence ratio deserves is needed in the future.

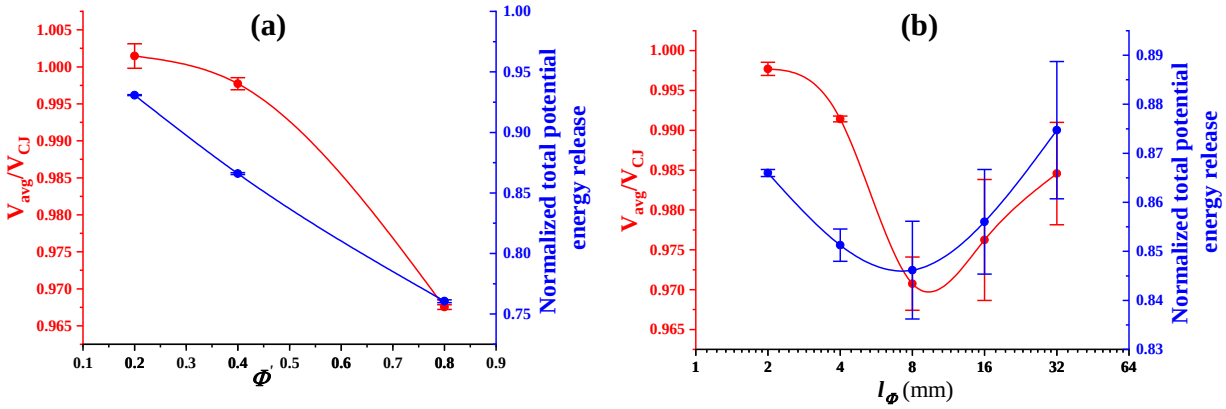

Fig. 8 The statistically normalized average velocity of detonation and rate of potential energy release as functions of (a) $\emptyset'$ and (b) $l_{\emptyset}$.

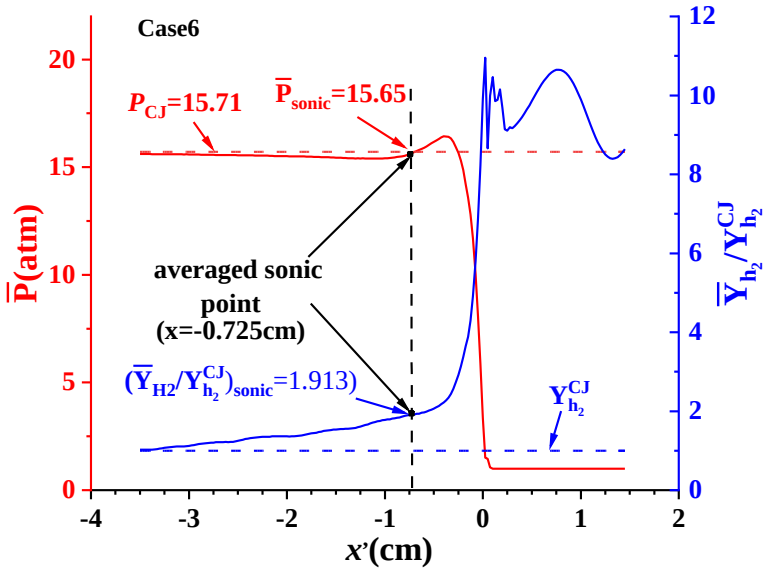

Fig. 9 1D Favre-averaged detonation profile for $l_{\emptyset} = 16$ mm.

4. Conclusions

This study investigated detonation propagation in a field with an inhomogeneous concentration by using a set of 2D simulations to consider the detailed reaction chemistry of the H_2/air mixture. The main conclusions are as follows:

First, the effects of the RMS $\emptyset'$ and the characteristic length scale $l_{\emptyset}$ of fluctuations in the equivalence ratio on the evolution of the cellular structure were evaluated. With an increase in $\emptyset'$ at

a fixed $l_{\emptyset}$, the cell sizes increased because some triple points weakened and even disappeared to decrease in number. A wrinkled wave front appeared at $\emptyset' = 0.8$ and a dense local explosion was triggered in this case. As $l_{\emptyset}$ was increased, the local explosion was promoted because of the enhanced curvature of the wave front, and increased the distance between the explosions. This in turn increased the cell size and facilitated the transition from a single cellular pattern to a double cellular pattern.

Second, the formation of the double cellular pattern was analyzed and the shock-induced pressure was calculated. There were three means for the formation of the large cell: (i) local explosion induced by the curvature of the wave front, (ii) local explosion induced by double-transverse wave collision, and (iii) the propagation of a single, strong transverse detonation. The triple points generated by these three means were much stronger than the original triple points, and could cause the local decoupled wave front to redetonate to satisfy an essential requirement for sustainable detonation propagation. Some triple points propagating along the stoichiometric region strengthened, and their collision with the triple points due to the explosion provided an additional guarantee of the survival of detonation.

Lastly, the instantaneous and the average speeds of detonation were calculated. The instantaneous speeds of detonation followed the trend of evolution of the normalized potential instantaneous energy release. The average detonation speed decreased with an increase in $\emptyset'$, but $l_{\emptyset}$ had a non-monotonic influence on this speed. Two factors were responsible for the speed of detonation: the potential energy release that can direct feed the detonation, and the extent of the real-time mixing of the extra H_2 and O_2 behind the shock.

Funding

This work was supported by the National Natural Science Foundation of China (Grant No. 51921004).

Acknowledgment

We thank Prof. Fan Zhang for providing information on initial fields of the equivalence ratio.

DATA AVAILABILITY

The data that support the findings of this study are available from the corresponding author upon reasonable request.

Appendix

A.1 Distributions of initial equivalence ratio

Fig. 10 shows the initial fields of the equivalence ratio for the cases considered in the simulations. All initial fields of the equivalence ratio were generated within a square of area 6.4 cm × 6.4 cm, and the inhomogeneous region consisted of two corresponding fields.

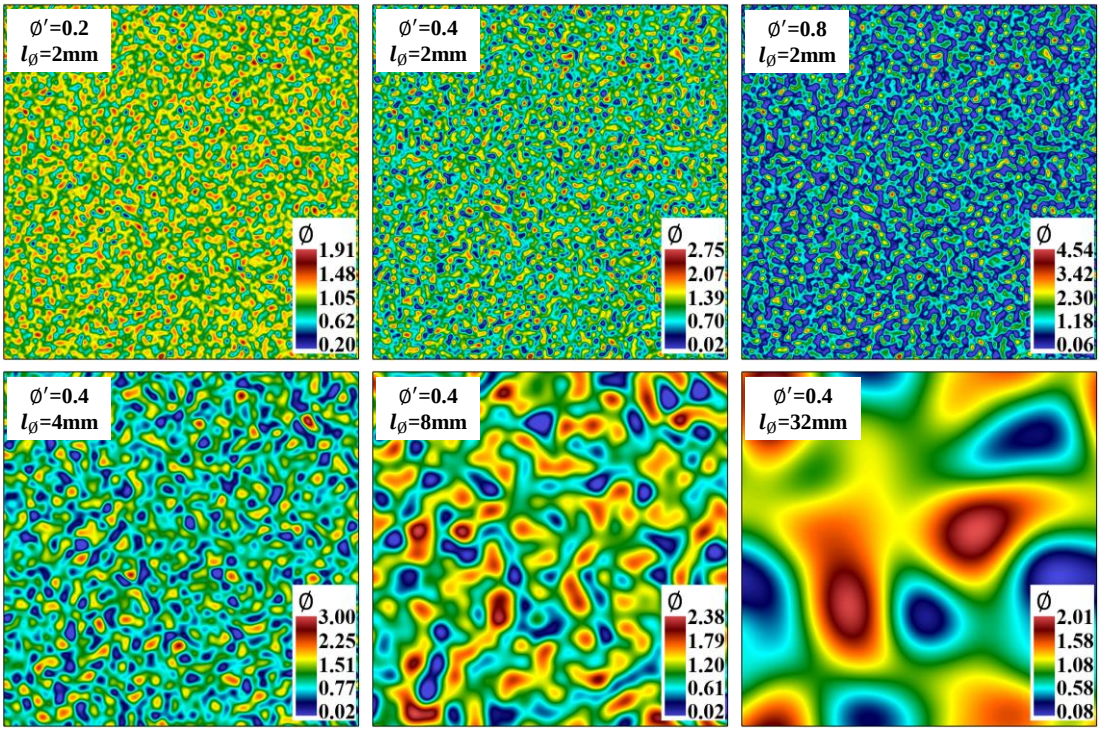

Fig. 10 Initial field of the equivalence ratio of the main cases considered in the simulations.

A.2 Grid resolution

A grid convergence test is performed for $l_\emptyset = 8$ mm with three levels of refinement as listed in **Table 2** to resolve the induction length with 12, 24, and 48 points. **Figs. 11** and **12** show the cellular structures of the homogenous and inhomogeneous region, respectively. The results did not show significant differences between them in terms of the overall cellular pattern, especially the double cellular structure and its formation, which suggests that the resolution was fine enough for our purposes. However, we cannot claim absolute convergence in light of the following two subtle details: One is that the cell size increased slightly from about 0.7 mm to 1 mm but this does not qualitatively affect the conclusions, as discussed in the next section. The second is that the original number of triple points decreased by more when the detonation barely entered the inhomogeneous region (about

X=7–9 cm), leaving a larger blank region within the larger cell, but a large number of substructures were recovered after this region. Thus, it seems that a longer "transition region" was needed for the detonation to adapt to inhomogeneity with a finer grid. However, the blank region is not a new phenomenon, and has been mentioned above when the detonation passed through the extremely lean region. Both details might be related to numerical diffusion, which can be reduced by using a finer grid for a slower energy release. This can weaken the ability of the detonation to propagate in limit conditions.

Table II Three types of meshes used in the simulations

Mesh	Mesh I	Mesh II	Mesh III
Finest mesh size	Five levels $250/2^4 \approx 15.6$ μm	Six levels $250/2^5 \approx 7.8$ μm	Seven levels $250/2^6 \approx 3.9$ μm
Points per unit induction length (pts/l_i)	12	24	48

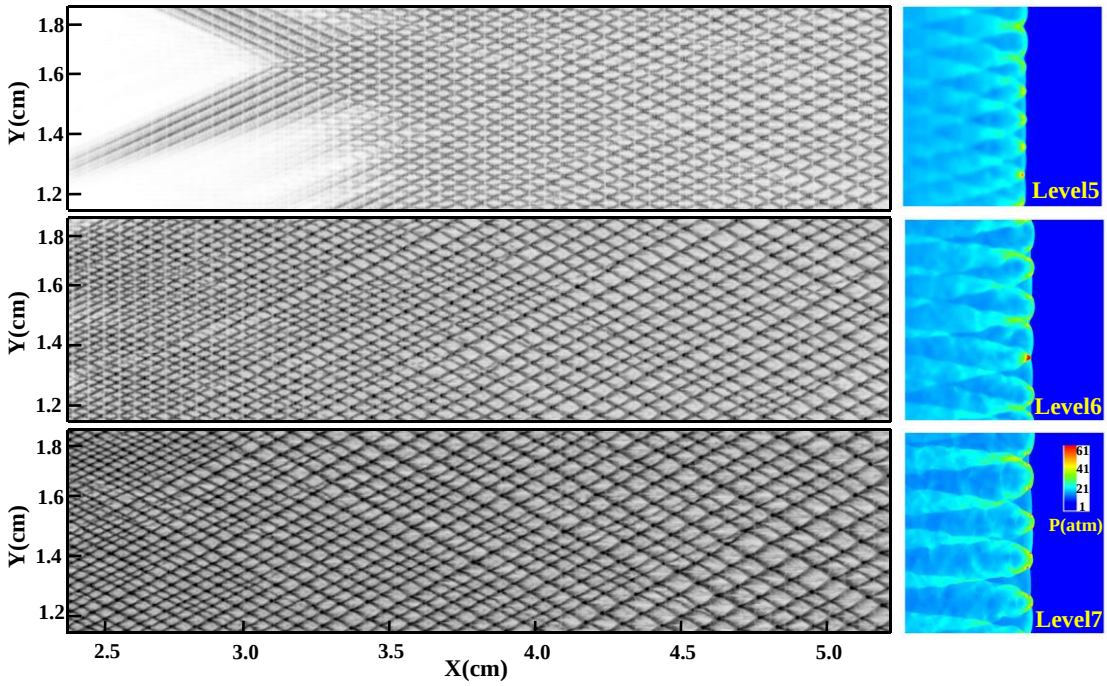

Fig. 11 Cellular structure and pressure contours at t=16.5 μs in the homogeneous region.

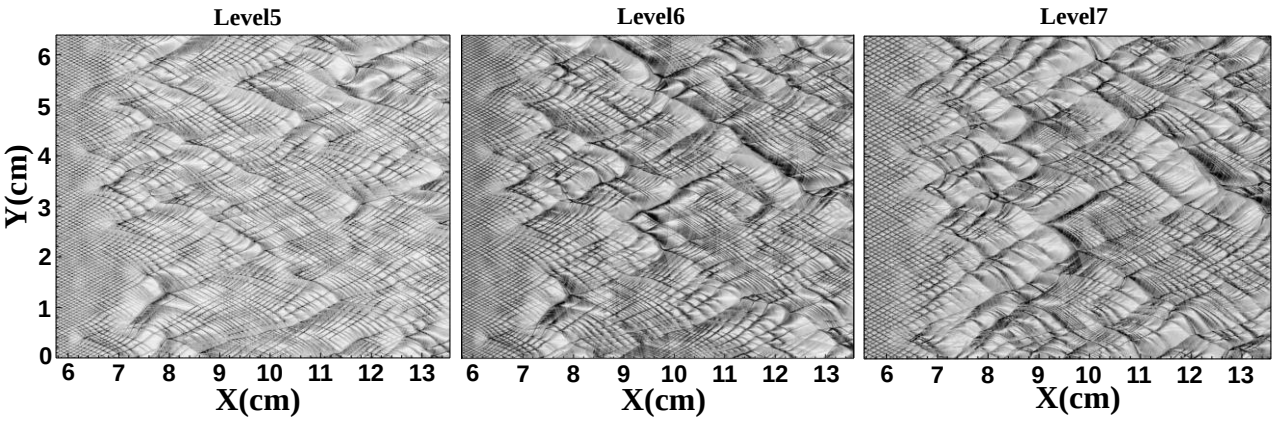

Fig. 12 Cellular structure in the inhomogeneous region.

A.3 Cell size

The accepted experimental error in the measurement of the detonation cell in a stoichiometric mixture of H_2/air at 300 K and 1 atm is approximately 10 mm, and is different from the results we obtained with the mechanism proposed by Li et al.[32]. Besides the aforementioned resolution effect, following observations are more important. (1) Heat losses to the wall in the experiments induced a larger cell.[40] (2) We tested the case with $l_{\emptyset} = 32$ with the Westbrook mechanism,[38] and this yielded a cell of size ~2 mm in the homogenous region, but the overall cellular pattern remained the same even in the inhomogeneous region as shown in **Fig. 13**. Sizes of 0.7–2 mm were also obtained in previous studies using at least four mechanisms.[32, 38, 41, 42] Shimizu[41] ha argued that the size of the detonation cell significantly depends on the pressure-dependent reaction. Even so, the largest cell size (~2 mm) with such a mechanism is comparable to our results. (3) Voelkel et al.[43] demonstrated that the cell size increases when vibrational non-equilibrium is considered (a factor of two in their work). Thus, comparing the cell sizes in terms of absolute values between the experiment and the simulation is still problematic. But we want to emphasize that the conclusions here were determined mostly by using the ratio ($l_{\emptyset}$) of the length scale of fluctuations in the intrinsic cell size rather than its absolute value. A small $l_{\emptyset}$ (<2 based on the results) only increased the original cell size while a large $l_{\emptyset}$ (>4) promoted the double cellular structure as analyzed here.

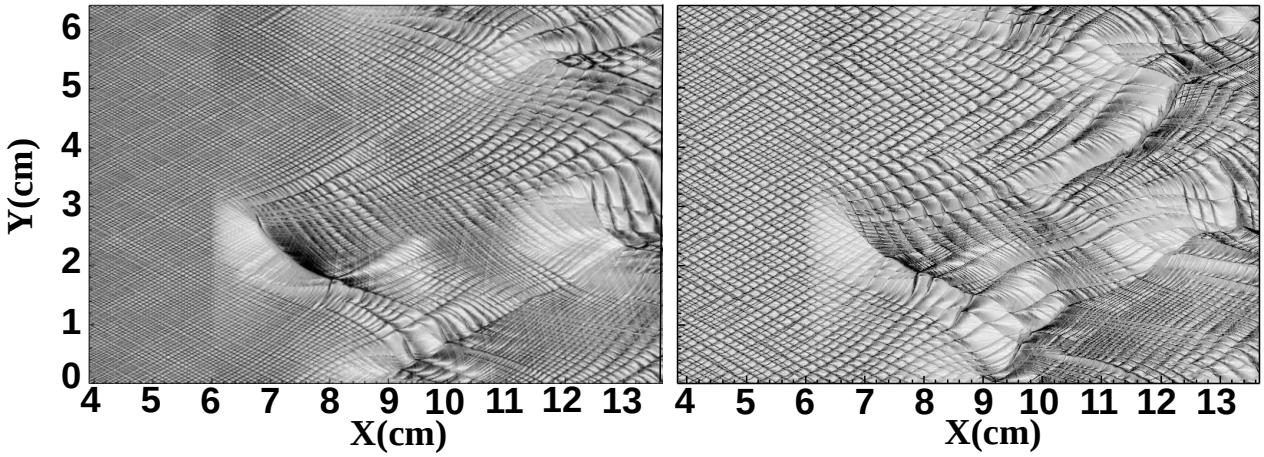

Fig. 13 Numerical soot foils for case 7 ($l_{\emptyset} = 32$ mm, $\emptyset' = 0.4$) with different mechanisms (the left shows the Li mechanism and the right the Westbrook mechanism).

Reference

1. A. Y. Poludnenko, J. Chambers, K. Ahmed, V. N. Gamezo, and B. D. Taylor, "A unified mechanism for unconfined deflagration-to-detonation transition in terrestrial chemical systems and type Ia supernovae," Science **366**, (2019).
2. J. Chambers, H. M. Chin, A. Y. Poludnenko, V. N. Gamezo, and K. A. Ahmed, "Spontaneous runaway of fast turbulent flames for turbulence-induced deflagration-to-detonation transition," Phys. Fluids **34**, 015114 (2022).
3. E. S. Oran, G. Chamberlain, and A. Pekalski, "Mechanisms and occurrence of detonations in vapor cloud explosions," Prog. Energy Combust. Sci. **77**, 100804 (2020).
4. S. Prakash, and V. Raman, "The effects of mixture preburning on detonation wave propagation," Proc. Combust. Inst. **38**, 3749 (2021).
5. Y. Liu, W. Zhou, Y. Yang, Z. Liu, and J. Wang, "Numerical study on the instabilities in H2-air rotating detonation engines," Phys. Fluids **30**, 046106 (2018).
6. Z. Wang, H. Liu, and R. D. Reitz, "Knocking combustion in spark-ignition engines," Prog. Energy Combust. **61**, 78 (2017).
7. Q. Meng, N. Zhao, and H. Zhang, "On the distributions of fuel droplets and in situ vapor in rotating detonation combustion with prevaporized n-heptane sprays," Phys. Fluids **33**, (2021).
8. S. Boulal, P. Vidal, and R. Zitoun, "Experimental investigation of detonation quenching in non-uniform compositions," Combust. Flame **172**, 222 (2016).
9. R. W. Houim, and R. T. Fievisohn, "The influence of acoustic impedance on gaseous layered detonations bounded by an inert gas," Combust. Flame **179**, 185 (2017).
10. K. C. Tang-Yuk, X. Mi, J. H. Lee, H. D. Ng, and R. Deiterding, "Transmission of a detonation wave across an inert layer," Combust. Flame **236**, 111769 (2022).
11. G. Thomas, P. Sutton, and D. Edwards, "The behavior of detonation waves at concentration gradients," Combust. Flame **84**, 312 (1991).
12. Y. Wang, C. Huang, R. Deiterding, H. Chen, and Z. Chen, "Propagation of gaseous detonation

across inert layers," Proc. Combust. Inst. **38**, 3555 (2021).
13. P. Honhar, C. R. Kaplan, R. W. Houim, and E. S. Oran, "Role of reactivity gradients in the survival, decay and reignition of methane-air detonations in large channels," Combust. Flame **222**, 152 (2020).
14. L. Boeck, F. Berger, J. Hasslberger, and T. Sattelmayer, "Detonation propagation in hydrogen–air mixtures with transverse concentration gradients," Shock Waves **26**, 181 (2016).
15. L. R. Boeck, J. Hasslberger, and T. Sattelmayer, "Flame acceleration in hydrogen/air mixtures with concentration gradients," Combust. Sci. Technol. **186**, 1650 (2014).
16. F. Ettner, K. Vollmer, and T. Sattelmayer, "Mach reflection in detonations propagating through a gas with a concentration gradient," Shock Waves **23**, 201 (2013).
17. K. Ishii, and M. Kojima, "Behavior of detonation propagation in mixtures with concentration gradients," Shock waves **17**, 95 (2007).
18. D. Kessler, V. Gamezo, and E. Oran, "Gas-phase detonation propagation in mixture composition gradients," Philosophical Transactions of the Royal Society A: Mathematical, Physical and Engineering Sciences **370**, 567 (2012).
19. W. Han, C. Wang, and C. K. Law, "Role of transversal concentration gradient in detonation propagation," J. Fluid Mech. **865**, 602 (2019).
20. M. Reynaud, F. Virot, and A. Chinnayya, "A computational study of the interaction of gaseous detonations with a compressible layer," Phys. Fluids **29**, 056101 (2017).
21. Y. Wang, Z. Chen, and H. Chen, "Propagation of gaseous detonation in spatially inhomogeneous mixtures," Phys. Fluids **33**, 116105 (2021).
22. X. Mi, A. J. Higgins, H. D. Ng, C. B. Kiyanda, and N. Nikiforakis, "Propagation of gaseous detonation waves in a spatially inhomogeneous reactive medium," Phys. Rev. Fluids **2**, 053201 (2017).
23. X. Mi, E. V. Timofeev, and A. J. Higgins, "Effect of spatial discretization of energy on detonation wave propagation," J. Fluid Mech. **817**, 306 (2017).
24. X. Mi, A. Higgins, C. Kiyanda, H. Ng, and N. Nikiforakis, "Effect of spatial inhomogeneities on detonation propagation with yielding confinement," Shock Waves **28**, 993 (2018).
25. A. Cuadra, C. Huete, and M. Vera, "Effect of equivalence ratio fluctuations on planar detonation discontinuities," J. Fluid Mech. **903**, (2020).
26. R. Yu, and X.-S. Bai, "A fully divergence-free method for generation of inhomogeneous and anisotropic turbulence with large spatial variation," J. Comput. Phys. **256**, 234 (2014).
27. R. H. Kraichnan, "Diffusion by a random velocity field," Phys. Fluids **13**, 22 (1970).
28. M. B. Luong, F. E. H. Pérez, and H. G. Im, "Prediction of ignition modes of NTC-fuel/air mixtures with temperature and concentration fluctuations," Combust. Flame **213**, 382 (2020).
29. C. S. Yoo, Z. Luo, T. Lu, H. Kim, and J. H. Chen, "A DNS study of ignition characteristics of a lean iso-octane/air mixture under HCCI and SACI conditions," Proc. Combust. Inst. **34**, 2985 (2013).
30. F. Zhang, R. Yu, and X.-S. Bai, "Direct numerical simulation of PRF70/air partially premixed combustion under IC engine conditions," Proc. Combust. Inst. **35**, 2975 (2015).
31. R. Deiterding, "A parallel adaptive method for simulating shock-induced combustion with detailed chemical kinetics in complex domains," Comput. Struct. **87**, 769 (2009).
32. J. Li, Z. Zhao, A. Kazakov, and F. L. Dryer, "An updated comprehensive kinetic model of

hydrogen combustion," Int. J. Chem. Kinet. **36**, 566 (2004).
33. X. Zhang, H. Wei, L. Zhou, X. Cai, and R. Deiterding, "Relationship of flame propagation and combustion mode transition of end-gas based on pressure wave in confined space," Combust. Flame **214**, 371 (2020).
34. H. Wei, X. Zhang, H. Zeng, R. Deiterding, J. Pan, and L. Zhou, "Mechanism of end-gas autoignition induced by flame-pressure interactions in confined space," Phys. Fluids **31**, 076106 (2019).
35. W. Chen, J. Liang, X. Cai, and Y. Mahmoudi, "Three-dimensional simulations of detonation propagation in circular tubes: Effects of jet initiation and wall reflection," Phys. Fluids **32**, 046104 (2020).
36. W. Zhao, J. Liang, R. Deiterding, X. Cai, and X. Wang, "Effect of transverse jet position on flame propagation regime," Phys. Fluids **33**, (2021).
37. K. Kaneshige, and J. Shepherd, "Detonation database, explosion dynamics laboratory report FM97-8," California Institute of Technology, Pasadena, CA (1999).
38. C. K. Westbrook, and F. L. Dryer, "Chemical kinetic modeling of hydrocarbon combustion," Prog. Energy Combust. **10**, 1 (1984).
39. M. I. Radulescu, G. J. Sharpe, C. K. Law, and J. H. Lee, "The hydrodynamic structure of unstable cellular detonations," J. Fluid Mech. **580**, 31 (2007).
40. Q. Xiao, and C. Weng, "Effect of losses on hydrogen–oxygen–argon detonation cell sizes," Phys. Fluids **33**, (2021).
41. H. Shimizu, A. Hayashi, and N. Tsuboi, *Study of detailed chemical reaction model of hydrogen-air detonation* (2001).
42. T. Sato, S. Voelkel, and V. Raman, *Detailed chemical kinetics based simulation of detonation-containing flows* (American Society of Mechanical Engineers, 2018).
43. S. Voelkel, D. Masselot, P. L. Varghese, and V. Raman, *Analysis of hydrogen-air detonation waves with vibrational nonequilibrium* (AIP Publishing LLC, 2016).